Advances in Engineering Software 42 (2011) 463–476

Contents lists available at ScienceDirect

Advances in Engineering Software

journal homepage: www.elsevier.com/locate/advengsoft

A computer model based on real anatomy for electrophysiology study

Weijia Lu [a,b], Daming Wei [a,c,*], Xin Zhu [a], Wenxi Chen [a]

[a] Biomedical Information Technology Lab, The University of Aizu, Fukushima Ken 965-8580, Japan
[b] Department of Healthcare, Philips Research Asia, Shanghai 200-233, China
[c] College of Computer Science, Hangzhou Dianzi University, Hangzhou, Zhejiang 310018, China

ARTICLE INFO

Article history:
Received 7 November 2010
Received in revised form 17 March 2011
Accepted 20 March 2011
Available online 11 April 2011

Keywords:
Computational model
Anatomic data discretization
Excitation simulation
Isochronal map
ECGs
Open source

ABSTRACT

In order to investigate the pattern of wave propagation on atria in both sinus rhythm and arrhythmia, we constructed a computational model based on real anatomy. The original anatomic data which encompasses morphological and geometrical knowledge was created from a whole-body set of 2 mm interval magnetic resonance imaging (MRI) images of a male volunteer and represented in stl format. The anatomic data was firstly discretized into spherical cells in equal size. Then the anisotropy of conduction velocity (CV) and conductivity were introduced into this model in definition of special conduction system. Nygren cell model was adopted to calculate the action potential (AP) waveform of each cell. Restitution of AP duration (APD) and it on CV were also introduced in this model. The pattern of activation propagation could be investigated on a perspective 3D scene after the excitation simulation. The isochronal map and the electrocardiograms (ECGs) were also produced. In this study, We used two experiments to verify this model as well as demonstrated its application in electrophysiological study: one was conducted under sinus rhythm, while in the other, two trains of boost pacings alternatively acted on the vena cava and the opening of the pulmonary vein. An identical excitation pattern described in previous studies was observed in first experiment. While in the second experiment, a foci triggered atrial fibrillation was seen on the epicardial surface.

1. Introduction

Atrial arrhythmia, the most common cardiac arrhythmia associated with increased mortality and substantial morbidity [1], can range in severity from annoying to life-threatening [2]. Computational modeling, with an arbitrarily high spatial resolution and a unlimited small simulation step, could provide hypothesis to be verified in experimental observations and do 'clean' experiments without much expense [3,4].

In 2000, Harrild and Henriquez produced an atria model of high atrial anatomical precision and the sinus rhythm was simulated [2]. In 2001, Vigmond et al. set up a morphologically realistic atria model which only contained the major structural features, and used it to simulate reentry propagation [5]. In 2006, Seemann et al. built an anatomically based model of the human atria that incorporated both structural and electrophysiological heterogeneities [6]. These models are superior because of huge numerous elements and special conduction systems defined on them [4], which represent how advanced the field of heart modeling has become [7]. However, Harrild's model and Vigmond's model are both directly composed from electrophysiological knowledge rather than raw anatomic clinic records [2,5]. This limits the universally application of these models in the cardiac arrhythmia study if a configurable resolution is essential to the simulation result.

The propagation simulation on the computational model with a large scale of realistic elements, named simulation cells in this study, suffers a heavy load of calculation if the Hodgkin–Huxley formula combined with reaction–diffusion theory is used in excitation simulation [8,9]. So a parallel computing technology, e.g. MPI, GPGPU, OpenMP, is usually adopted in this situation, but it increases the difficulty of implementation and deployment [2,6]. On the other hand, the computational model based on Huygens's principle, like Wei–Harumi model, can simulate complex ventricle arrhythmia precisely without a long calculating period [10–12]. However Wei–Harumi model has not enough sum of simulation cells in atria compared with other computational models and no special conduction system.

In this study, a suite of computational modeling and simulation tools is described. These tools could partition anatomical record into a large scale of simulation elements (in the simulation introduced here, there are over 350,000 elements). Special conduction system in other models [2,5,6], which is absent in Wei–Harumi model, could also be defined. Anisotropic cellular automaton could be assigned to each simulation cell by the formulation in Nygren et al.'s study [13]. After the whole model is prepared, the excitation simulation based on Huygens's principle could be conducted. And

* Corresponding author at: College of Computer Science, Hangzhou Dianzi University, Hangzhou, Zhejiang 310018, China. Tel.: +86 21 24127319.
E-mail address: AlfredWJLu@gmail.com (W. Lu).

0965-9978/$ - see front matter © 2011 Elsevier Ltd. All rights reserved.
doi:10.1016/j.advengsoft.2011.03.015

ECGs missing in other models could also be calculated [2,5,6]. In the later part of this study, two experiments are conducted to verify the whole model as well as to demonstrate the application of this model in electrophysiological study. In a word, the computational model and corresponding software tools, the details of which are described in following sections, inherits from other excellent computational models [2,5,6,10], and provides a well designed platform for electrophysiological study.

2. Methods

2.1. Generation of simulation cells from atrial anatomic data

The raw atrial anatomic data used in this study comes from a whole-body set of 2 mm interval MRI images of a male volunteer [14]. It is represented in a stl file which describes a raw unstructured triangulated surface by the unit normal and vertices (ordered by the right-hand rule) in a three-dimensional Cartesian coordinate system.

The raw anatomic data constructed of many triangulate mesh in stl file is then put into an oblique coordinate system with equal axis angles of 60° as in Wei–Harumi model [10]. Then the spherical simulation union named simulation cell is discretized and its radius is recorded in the configure file for further simulation. In the process of discretization of the anatomic data, the including test of each simulation cell to the atrium myocardium is fulfilled by the solid angle calculating proposed by Opstream et al.'s study [15]. A binary hrt file is produced after the discretization to mark the types of all simulation cells in this oblique coordinate system. Fig. 1a shows the anatomic data we use and Fig. 1b displays the discretization result. This method can be arbitrarily adopted on discretization of any anatomic data in stl format, see Fig. 1c and d for ventricle case.

2.2. Definition of conduction system in the simulation cells set

Because the set of simulation cells is directly generated from anatomical records, some of the anatomic features such as the openings of veins, atrial–ventricle (AV) valves, taenia terminalis and coronary sinus (CS) can be clearly investigated in it (see Fig. 1a). But special conduction structures, which are embedded in the atrium myocardium and might be the substrates of the arrhythmia, are not involved in the mesh representation in the original anatomic data. Therefore, these structures, including sinus node (SN), bachmann bundle (BB), fossa ovalis limbus (FOL), fossa ovalis (FO), pectinate muscle (Pects), crista terminalis (CT), intercaval bundle (IB) and right atria floor isthmus (Isthmus) [2,5,6], have to be manually defined by assigning a certain type to each simulation cell in the cross-section of simulation cells set (see Fig. 2a–f for its perspective view). The measurements of these conduction structures are approximately summarized in Table 1. The location and orientation of each component of special conduction system are the same as in Harrild model [2]. The binary hrt file is updated when special conduction is assigned.

2.3. Generation of AP waveform of each simulation cell

Instead of linear approximation of AP waveform by a set of geometrical parameters in Wei–Harumi model [10], here AP is generated based on the Nygren model [13]. This human atrial cell model has 29 variables to determine total twelve transmembrane currents. Fig. 3 shows the AP waveform used in our simulation. The benefit of using Nygren model is : the parameters in Nygren model precisely correspond to the ionic parameters in the physical cell membrane, which could be accurately measured in clinic experiment, so different anatomic regions could be defined with one or two parameters of Nygren model shifting according to the clinic record, in this way the real distribution of AP on atrial myocardium in some realistic condition, e.g. drug therapy in AF, could be simulated and the result of subsequent simulation is more credible.

2.4. Introduction of APD restitution and CV restitution

The APD of cardiac myocardium is known to depend on the length of the preceding diastolic interval (DI) in a relationship termed 'APD restitution' [16–18]. In our simulation, the unimodal restitution described in Ronald's study is used Eq. (1) [16].

$$APD(DI) = 150 - 0.5e^{-\frac{DI-600}{100}} \tag{1}$$

In sinus case, if the cycle length (CL) is equal to 600 ms, with this restitution waveform, the APD is kept in 147 ms, and DI is in 453 ms.

The preceding DI also influences the conductivity velocity, which is known as the 'CV restitution'. This effect is mainly based on the conductivity reduction due to the decrease in connexin 40 (CX40) or the decrease in the resting membrane voltage [19]. In our simulation, CV is defined in three catalogs as the function of the preceding DI: bulk (Eq. (2)), bundle (Eq. (3)) and slowregion (Eq. (4)) and determined by the cell type of both source and destination.

$$CV(DI) = 6.125 - 0.5e^{-\frac{DI-600}{300}} \tag{2}$$

$$CV(DI) = 46.22 - 0.005e^{-\frac{DI-600}{50}} \tag{3}$$

$$CV(DI) = 1.86 - 0.5e^{-\frac{DI-600}{500}} \tag{4}$$

The bundle speed only exists between two cells in these special conduction structures: Pects, CT, IB, BB, FOL and SN; the slowregion speed only exists between two cells: FO and Isthmus, and propagations between most of simulation cells are conducted in bulk speed. The morphologies of the CV restitution waveforms are compatible with the counterparts in both Gong et al.'s study [20] and Xie et al.'s study [21].

2.5. Simulation of activation propagation

The activation propagation in a computational model could be described either in Huygens's principle or the reaction-diffusion formula. The latter one has the capability to respond to changes in conductivity, ionic current etc. But the complexity of such models usually induces a heavy calculation. The propagation simulation in our model relies on the Huygens's principle, i.e. every cell on the activation wave front may be treated as the source of secondary wavelets that spread out in all directions.

In our simulation, cells are divided into two types: autonomic and nonautonomic. Autonomic cells including the paced cells or the cells which can excite themselves at the phase IV on AP waveform (e.g. SN). Nonautonomic cells indicate the cells which cannot be excited until the conductive activation arrives. The propagation simulation is discretized into constant time span of 1 ms, and proceeds under following rules.

1. All nonautonomic cells and some of autonomic cells (the paced cells) can be excited.
2. The activation on a cell can spread to its neighbor. In our oblique coordinate system, there are twelve neighbors around one cell after the discretization.
3. The AP waveform is generated before the propagation simulation by the manner introduced in Section 2.3. The entire AP waveform is then divided into four parts: phase I, II, III, IV. See Fig. 3. The APD restitution only effect phase II and III,

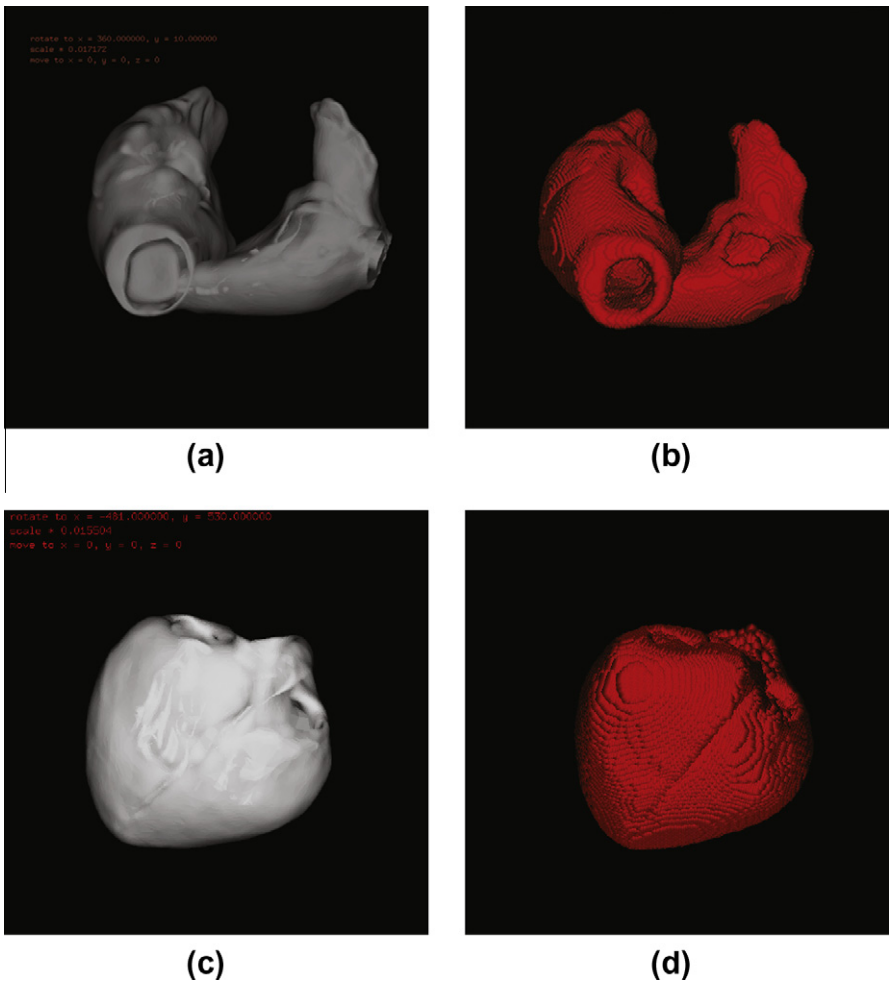

Fig. 1. (a) Represent the original anatomic data of atria (aorta and pulmonary artery are not initially included) and (b) represent the discretization result (or named simulation cells set in this paper), each little spheroid denotes one simulation unit. (c) and (d) Demonstrate the original anatomic data and discretization result of ventricle respectively.

because the Nygren model is used in our simulation. This attribution of Nygren model is heavily described in Cherry et al.'s study [22].

4. The cell is capable to excite its neighbor if and only if its membrane voltage falls in phase I.
5. The cell is capable to be excited if its membrane voltage is in phase III and phase IV.
6. The cell is said to be in activation status if its membrane voltage is in phase I and phase II.
7. The cell is said to be in deactivation status if its membrane voltage is in phase III and phase IV.
8. Although the simulation processing is discretized into constant time span, the propagation of activation among cells is continuous. Precisely speaking, the location of wave front in latest step is recorded temporarily and recovered in the new step.

After the propagation simulation is completed, the propagation process can be investigated in a vivid 3D scene with colorful marks of activated simulation cells in each step, and the isochronal map can also be generated.

2.6. Calculation of ECGs based on the result of propagation simulation

The extracellular potential field, which drives the body surface ECG, arises from the transmembrane currents and therefore is linked to the transmembrane potentials. And the human tissue is a volume conductor whose capacitive reactance can be ignored according to Schwan's study [23]. So the extracellular potential field, which should be a static field, could be accessible when the conductivity of tissue is known [24]. See Eq. (5) for the calculation of the current dipole moment per unit volume, where $\vec{\sigma}$ denotes the conductivity tensor and $\nabla\Phi$ denotes the divergence of the potential field Φ. To get a current dipole, entrywise product should be used here instead of cross product.

$$\vec{J} = \vec{\sigma} \circ \vec{E} = -\vec{\sigma} \circ \nabla\Phi \tag{5}$$

The radius of simulation cell is 1.8586 mm in this computational model, while the radius of a tissue cell is about $10 - 100$ μm. It indicates that both intracellular space and the intercellular space, interconnected throughout the cardiac tissue, could be considered with average parameters in each simulation cell. Therefore bidomain theory becomes adaptable in our simulation [25]. According to this theory, any point in the simulation cell can be considered either in the intracellular space or in the intercellular space separated by a membrane of zero thickness. Moreover the conductivity tensor in these two domains could be considered as the same in a certain simulation cell determined by the cell type of both source and destination. If $\vec{\sigma}_i$ and $\vec{\sigma}_e$ denote the conductivity in intracellular space and intercellular space respectively, and so as the Φ_i and Φ_e, then Eq. (5) could be rewritten as follows.

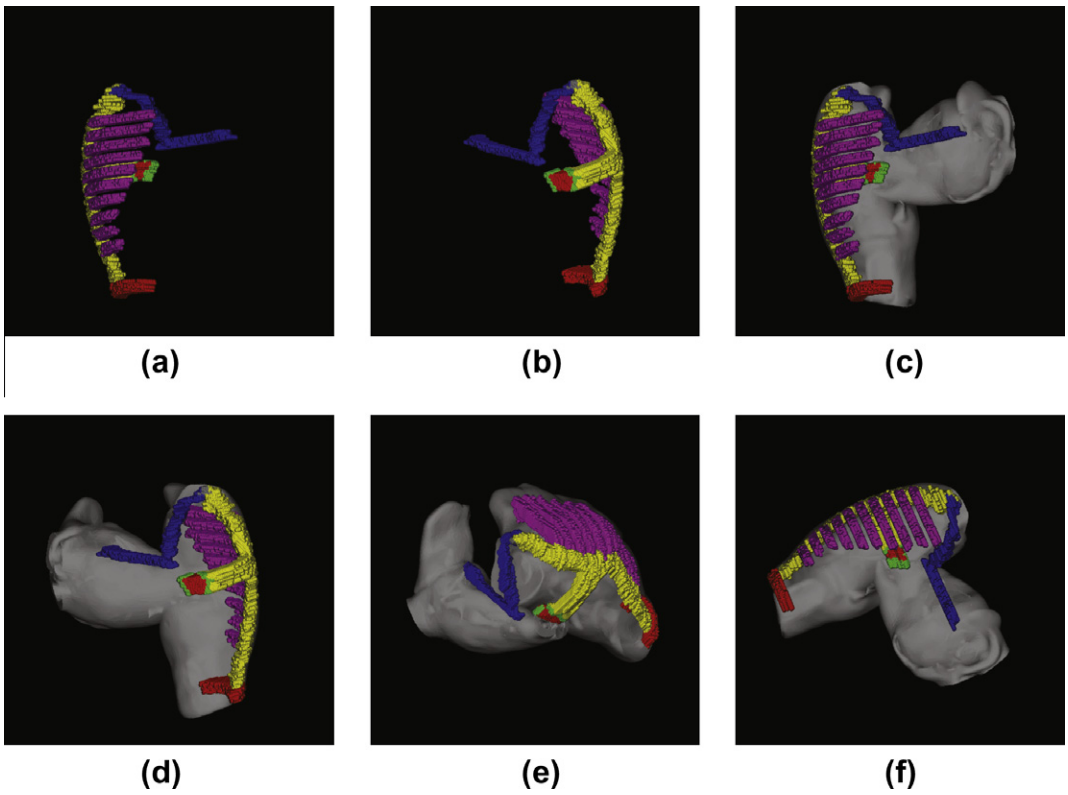

Fig. 2. (a) and (b) Give the special conduction system used in our simulation and (c)–(f) give the perspective description of these fibers in anatomic data. Special conduction mainly contains SN (little gray part connected BB and CT), BB (blue fiber), FOL (green fiber in circle), FO (red parts in FOL), Pects (purple), CT (yellow fiber connected all Pects), IB (yellow fiber connected FOL and CT) and Isthmus (red parts at the bottom of right atrium). (For interpretation of the references to color in this figure legend, the reader is referred to the web version of this article.)

Table 1
Geometrical measurements of special conduction structures in our model.

Name	Cross-section size (cm)	Length (cm)	Number
CT	Diameter = 0.296–0.333	2.56	1
IB	Diameter = 0.148–0.259	1.11–1.221	1
Isthmus	(0.296–0.37) × 0.259	1.258	1
Pects	(0.111-0.296) × 0.185	0.74–1.48	10
BB	Diameter = 0.074–0.259	1.665–1.85	1
SN	0.111 × 0.296	0.185	1

$$\begin{cases} \vec{J}_i = -\vec{\sigma}_i \circ \nabla \Phi_i \\ \vec{J}_e = -\vec{\sigma}_e \circ \nabla \Phi_e \end{cases} \tag{6}$$

$\vec{\sigma}_i$ and $\vec{\sigma}_e$ could be equal as mentioned before, so we have

$$\vec{J}_m = -\vec{\sigma} \circ \nabla \Phi_m \tag{7}$$

where $\vec{J}_m$ is the transmembrane current dipole, and Φ_m is the cross membrane voltage (i.e. the AP). The current source I_v can then be calculated as

$$I_v = \nabla \cdot \vec{J}_m \tag{8}$$

With Eqs. (7) and (8), we can see the voltage on the torso space and the current source satisfy Poisson's equation. σ here denotes the average conductivity in three parts: human tissue (0.002 mS/cm), blood (0.006 mS/cm) and torso (0.00125 mS/cm) [26].

$$\nabla^2 \Phi = -\frac{I_v}{\sigma} \tag{9}$$

The solution of Poisson's equation in a infinite space is

$$\Phi^{\infty}(r) = \frac{I_v}{4\pi\sigma r} \tag{10}$$

where r is the distance from the current source to a destination point where the ECG lead located on the torso. After that, we sum up the contribution of all the current sources to get the ECGs voltage on this lead in infinite medium in a certain simulation step.

To get the 'real' potential on torso leads, a boundary element based method introduced in Aoki et al.'s study is used [27]. If $\Phi(r)$ depicts the 'real' potential at point r, we have $\Psi r = \Phi(r) - \Phi^{\infty}(r)$, which should also satisfies the Laplace equation, here we rewrite Laplace equation in loose former

$$\int_{\Omega} dv(\nabla^2 \Psi)\omega = 0 \tag{11}$$

and if we use Green–Gauss function in this equation, we have

$$\int_{\Omega} dv(\nabla^2 \Psi)\omega + \int_{\Omega} dv(\nabla\omega)(\nabla\Psi) = \int_{\Omega} dv(\nabla\omega)(\nabla\Psi) = \int_{\Gamma} ds(\omega)\frac{\partial \Psi}{\partial \eta} \tag{12}$$

and we use Green–Gauss function in left hand again, we have

$$\int_{\Gamma} ds(\Psi)\frac{\partial \omega}{\partial \eta} - \int_{\Omega} dv(\nabla^2\omega)\Psi = \int_{\Gamma} ds(\omega)\frac{\partial \Psi}{\partial \eta} \tag{13}$$

If we use the Green's function as the weight $\omega \triangleq G(r, r') = \frac{1}{4\pi|r-r'|}$, we further have

$$\int_{\Gamma} ds(\Psi)\frac{\partial G}{\partial \eta} = \int_{\Gamma} ds(G)\frac{\partial \Psi}{\partial \eta} \tag{14}$$

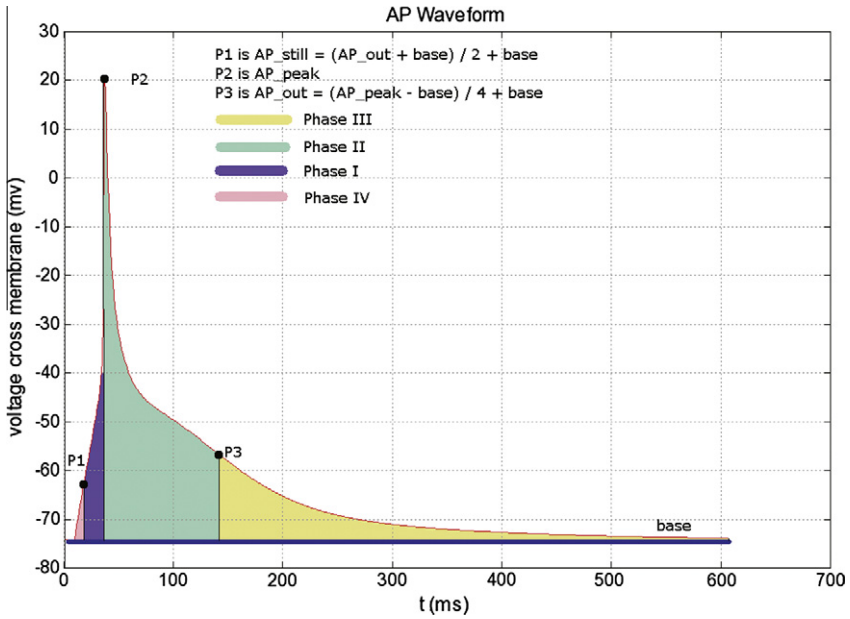

Fig. 3. AP waveform used in sinus simulation.

We impose both the Dirichlet boundary (Ψ) and Neumann boundary $\left(\frac{\partial \Psi}{\partial \eta}|_{\Gamma} = q^{\infty}\right)$, do transform introduced in Aoki et al.'s study, we have the finally equation for calculating 'real' potential

$$\Phi = \Phi^{\infty} - (H^t H)^{-1} H^t G q^{\infty} - (H^t H)^{-1} H^t a \tag{15}$$

3. Technology

The software suite created for our computational electrophysiological simulation includes four utilities: slicer, hrtEditor, solver and viewer, and the behavior of them can be configured in a configuration file. Slicer can generate simulation cells from a raw anatomic data. HrtEditor can investigate discretization result in cross-section manner after simulation cell set is generated, define the cell types and set the pacing profile for the simulation. Solver fulfills all simulation tasks, i.e. generating AP waveform, simulating the activation propagation in discretized simulation steps, calculating the current source and estimating epicardial potential distributions as well as the surface ECGs. Viewer, as its name indicates, can investigate raw anatomic data, simulation cell set, special condition system, activation propagation procedure and etc. The AP waveform and the surface ECGs can be visualized through some interactive gnuplot [28] script. See Fig. 4 for the

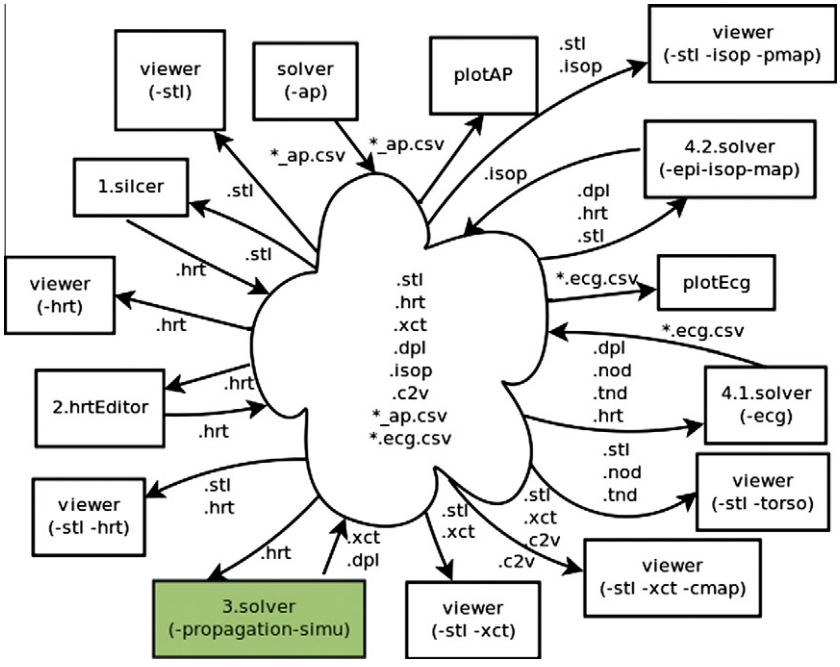

Fig. 4. The standard work flow and the cooperation of all utilities in a simulation session. The cloud stands for the set of all files corresponding to the simulation. Every rectangle indicates one process of a certain utility. Rectangles with a number are essential steps for one simulation session, while others are optional. The arguments for each process are showed in bracket in the corresponded rectangle. The numbers in essential steps indicate a invoking sequence. In the left hand of each arrow, all types of files for this process are listed, while in the right hand, files produced or updated in this process are listed. The details of colored process are described in Figs. 5 and 6.

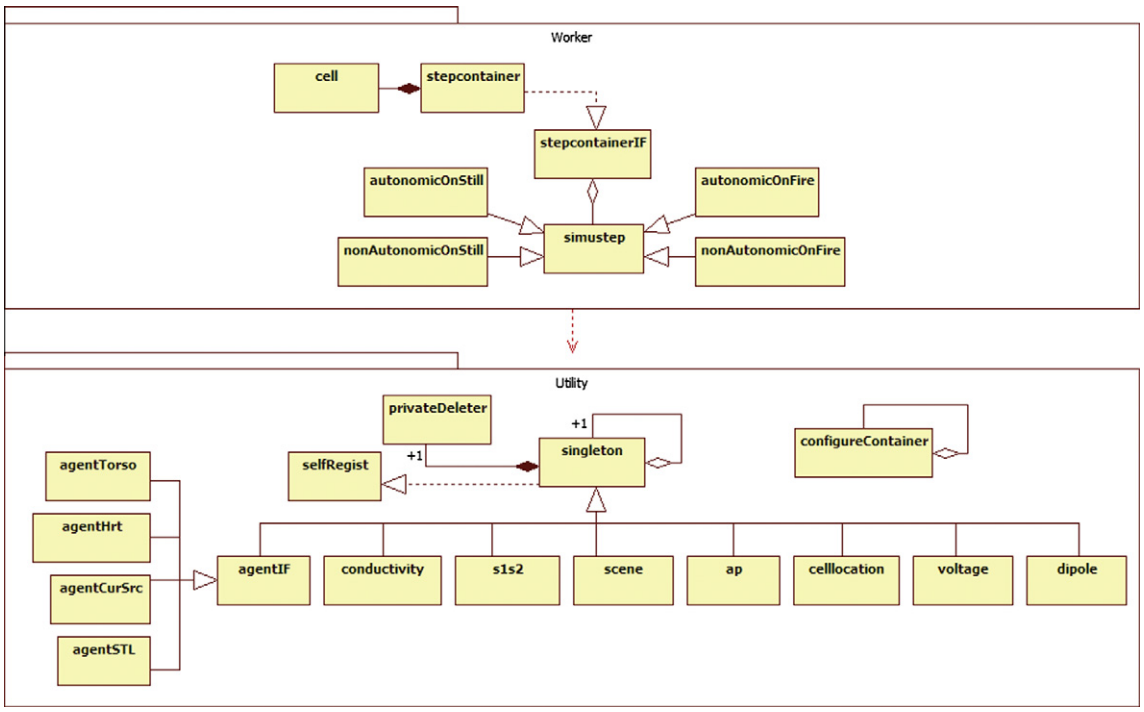

Fig. 5. Components diagram of solver.

standard work flow and the cooperation of all utilities in a simulation session.

All utilities are written in C/C++ language. To guarantee the high portability, only libraries encapsulated in C/C++ standard and state-of-art Graphic User Interface (GUI) libraries (in our case, they are GTK libraries [29] and OpenGL libraries [30]), are used in the implementation of these utilities. To make the deployment of these utilities more convenient, sources of these utilities are distributed under the GPL license [31], maintained by GNU GCC [32] with carefully designed make file [33].

The components of solver are presented in Figs. 5, and 6 gives essential activities in a simulation. The packet named utility in solver provides many static methods to be invoked by the members in worker packet, and the latter one determines the simulation processing. The class named singleton, from which all classes in utility packet inherit, is designed as a Singleton [34] with self-register and private destruction. The classes inherited from agentIF focus on I/O for different file types in the simulation, e.g. agentHrt for .hrt file. And the functionality, fulfilled by other classes directly inherited from the singleton, can be easily guessed from its name:

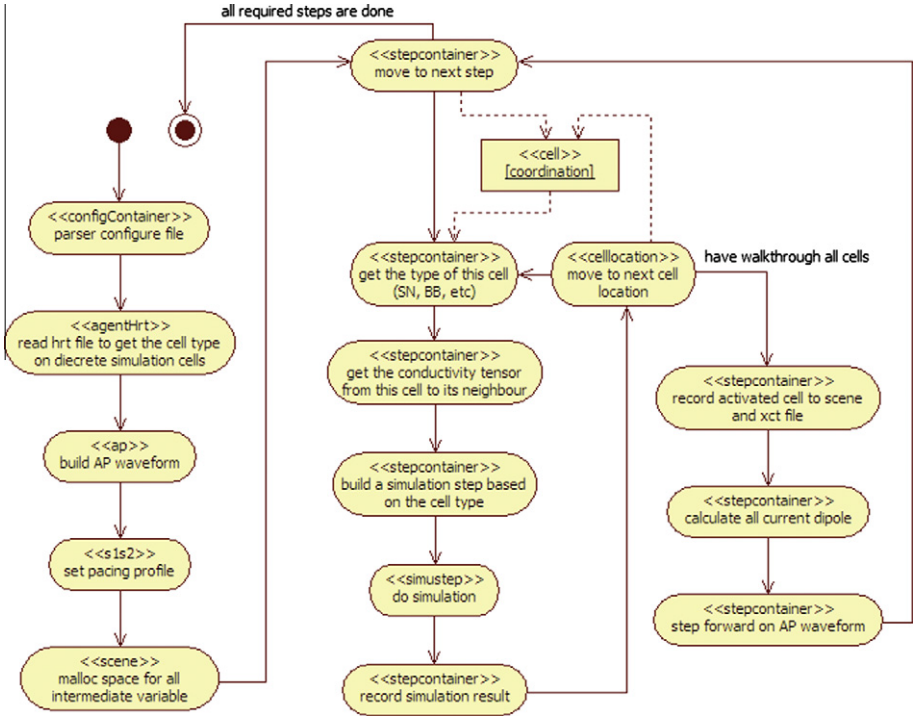

Fig. 6. Activities in a instance of propagation simulation.

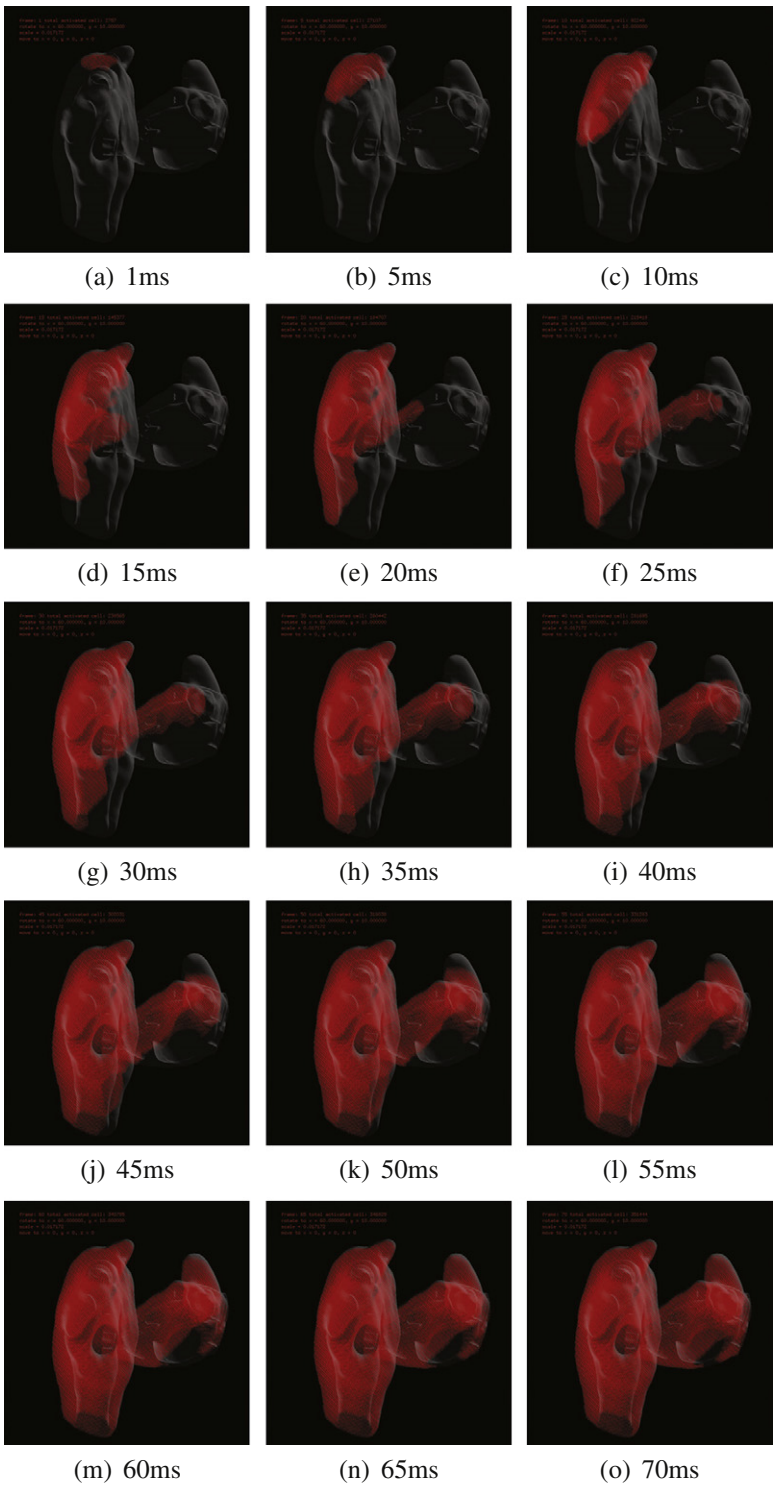

Fig. 7. (a)–(o) Denotes the propagation of activation in a perspective manner from 1 ms to 70 ms in 5 ms step, which can be got by using viewer with -stl -xct arguments. This kind of propagation investigation manner is named perspective propagation investigation in this study.

conductivity keeps the conduction velocity and the conductance; s1s2 keeps the profile of pacing and sinus excitation; dipole for current source calculation; celllocation maintains the coordination of each simulation cell; voltage for the potential calculating on the mesh triangle; ap maintains the AP waveform and scene keeps the intermediate variables.

The discretization scale in each axis of our oblique coordination system is 200. As for a 32-bit operation system, the capacity of memory space in user mode is usually less than 1.5 Gbytes. If individual memory space is defined to store status for each simulation cell throughout the simulation, it should be less than $1.5\,G/200^3 \approx 200$ bytes. Suppose the size of status information in each simulation cell is 4 bytes (in most platform, it is the size of a float variable), one simulation session could only contain less than 50 steps. To bypass this memory restriction of the operation system, a new simulation

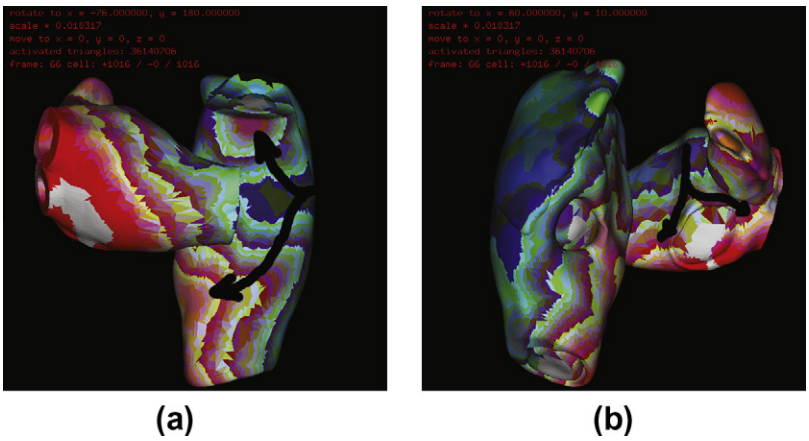

Fig. 8. (a) and (b) Give isochronal maps (posterior and frontal respectively) of wavefront propagation (1–66 ms), which can be got by using viewer with -stl -xct -cmap arguments. The direction of propagation is indicated by bold arrow, and a particular pseudo-colormap is used to differ the location of wavefront in each simulation step.

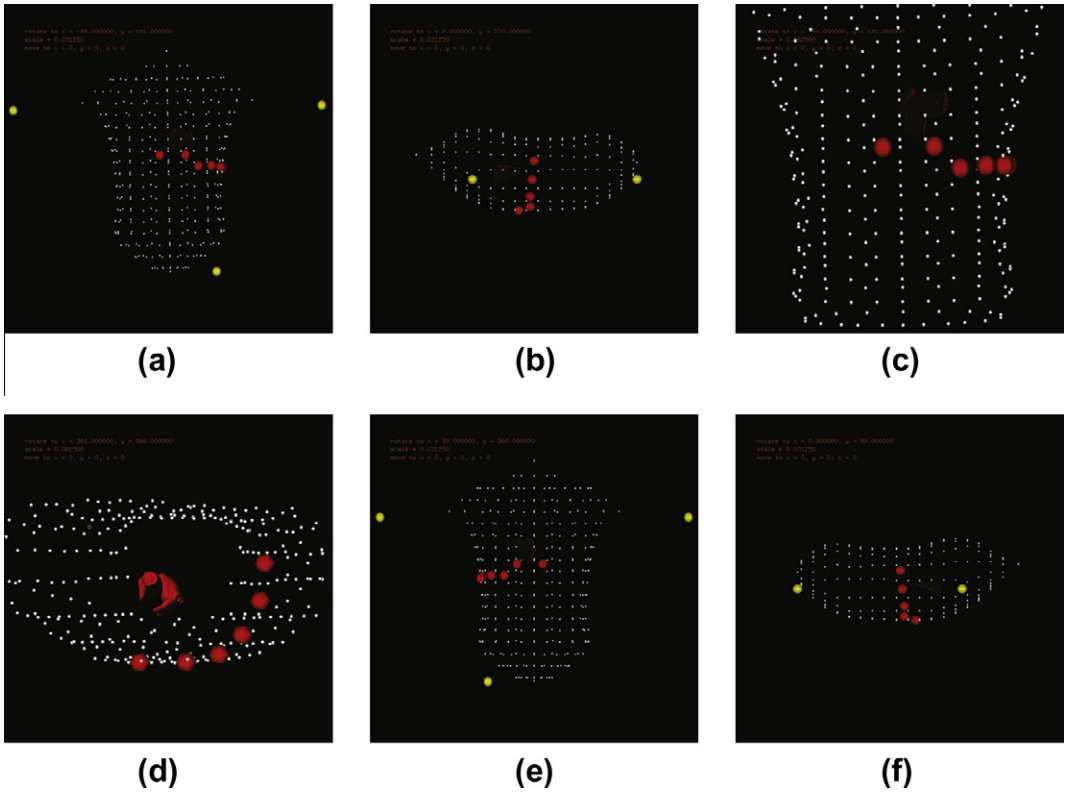

Fig. 9. (a)–(f) Give the torso model (each vertex on this model is represented as little silver spheres, the details of this model could be found in Wei's study [10]), atrium location and ECG electrode location used in simulation (limb leads in yellow spheres and precordial lead in red spheres). (For interpretation of the references to color in this figure legend, the reader is referred to the web version of this article.)

step is generated dynamically in every time step (see the iteration in Fig. 6 and the corresponding class in worker packet Fig. 5).

4. Simulation protocol and result

4.1. Sinus rhythm

Firstly, simulation in sinus rhythm is conducted to verify the whole system. The activation propagation is demonstrated in Fig. 7a–o, and the isochronal map in Fig. 8a and b.

As shown in Fig. 7b (5 ms) and c (10 ms), the wave initially quickly spreads anterior to the superior vena cava (SVC) and becomes nearly triangular as the crista activation precedes. This phenomenon is observed by the end of 20 ms in Harrild model [2]. In Fig. 7e (20 ms), almost the whole septal surface is activated and the depolarizing wave has now traversed the interatrial Bachmann's bundle, which happens in 29.7 ms in Harrild model [2]. In Fig. 7j (45 ms), the impulse starts to activate the left atrium appendage, which is in 50 ms in Harrild model [2]. And a small inactive bridge of tissue, which abuts against the mitral annulus in the lateral inferior left atrium, is last activated both in our simulation (see the white blank in Fig. 8a, starts from 66 ms) and in

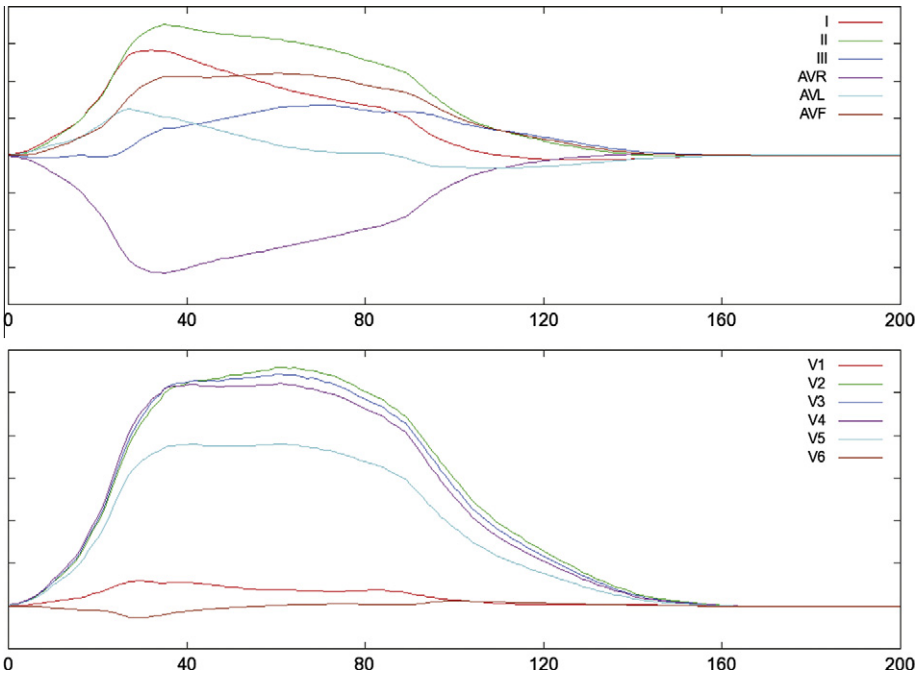

Fig. 10. ECGs waveform in limb leads (I, II, III, AVR, AVL, AVF) and precordial leads (V1–V6) in sinus rhythm. *X* axis denotes time in ms.

Table 2
Pacing configuration in the AF simulation.

Pacing location	S1	S2	S3	S4	S5	S6
RSPV	100	200	299	397	494	590
IVC	120	210	300	390	480	570

simulation result of Harrild model (starts from 100 ms) [2]. Such a sequence of activation propagation is also described in Durrer's study according to the clinic measurements [35].

In isochronal map, the contribution of the anisotropy of the crista to the propagation pattern, which is described in Harrild et al.'s study, could be clearly investigated (see Fig. 8b). In Fig. 8a with manually marks, the bifurcation of impulse could be seen on the free wall of right atrium, which is not reported in Harrild's study.

Furthermore, twelve leads ECGs are calculated in the simulation. After properly depositing the atria in a torso volume, and placing leads according to normal ECGs measurement condition [36], ECGs are obtained by summing up contribution of all current sources in each time step. The torso volume, the leads and the atria are displayed in Fig. 9a–f while the ECGs waveforms are in Fig. 10. ECGs waveform got in the simulation are in accord with some common principles used in ECG diagnosis: (a) The P wave duration (PWD) is in 0.12 –0.16 s [37]; (b) the P wave amplitude on lead III is smaller than that on lead I and II; (c) negative P wave appears on AVR lead [36]; and (d) the P waves on V2 and V3 are larger than those on other precordial leads because the cardiac apex is orientated to them.

4.2. Atrial fibrillation

In this experiment, two train of boost stimulations are conducted alternatively on the right superior pulmonary vein (RSPV, S1) and on the inferior vena cava (IVC, S2) (see Table 2 for pacing configuration in this simulation). A propagation simulation with overall length of 2000 ms is performed and the ECGs are calculated (see Fig. 1 for detail setting in this simulation).

The isochronal maps in Fig. 12a–u describe a spontaneous reentry propagation initiated from several ectopic foci (or can be internal reentry). The isochronal maps in Fig. 13a–m describe the morphology of this main reentry which drives the AF retrieved from the simulation. The ECGs waveforms are in Fig. 11.

Fig. 12a–c describe the propagation of the activation initialized by the pacing pair near 200 ms. From these isochronal maps, we can see the wave coming from the right atrial posterior region (PRA) meets the wave from the IVC almost near the IVC (in Fig. 12b), and disappears near the atrioventricular valve (in Fig. 12c). Then the pacing pair near 390 ms comes, which propagates much slower comparing with the counterparts initialized near 200 ms. For instance, if we take a look at the Fig. 12a and b, the wave activates around 3/4 of the right atrium in 20 ms. While in the cycle initialized from 390 ms, the wave only activates the right atrium appendage (ARA) (in Fig. 12e–g). This phenomenon indicates the gradient of the CV on the right atrium, which is caused by the boost pacing profile.

The main reentry near the tricuspid valve is firstly trigger by some ectopic foci on the ARA (see in Fig. 12j, k and p), These foci accelerate the wave propagation on the right atrium and finally generate an anticlockwise loop. These foci then disappear since the reentry is formed, so this onset of AF could be titled as 'foci triggered'. On the other hand, some other 'foci' keep showing up, e.g. 817 ms in Fig. 12t and 1049 ms in Fig. 13a. These foci do not contribute to the propagation pattern, because they are behind the wavefront. As they emerge in each loop, and settle in the same location on the ARA, we could say these 'foci' correspond to some internal macro or micro reentry.

Fig. 13a–m demonstrate the propagation pattern of the main loop in this onset of AF retrieved from the simulation. On the PRA, the wave travels longitudinally from the superior vena cava (SVC) to IVC (see Fig. 13e, g and i). On the other side of the right atrium, the wave coming back from the IVC (see Fig. 13b, d and l) collides with the wave on ARA (see Fig. 13f), then turns round near the tricuspid valve (see Fig. 13h), and fulfills one loop. On the left atrium, the wave goes horizontally, from right pulmonary veins to left pulmonary veins, and finally activates the left atrial appendage (ALA).

```
simulation = (
        ap = (
                model = nygren_atrial_model_1998
        )
        step = (
                units = ms
                val = 1.0
                sum = 2000
        )
        conductivity = (
                velocity = (
                        units = mm/ms
                        bulk = 6.125
                        bundle = 46.22
                        slowregion = 1.86
                )
                conductance = (
                        units = mS/mm
                        bulk = 1.202
                        bundle = 9.07
                        slowregion = 0.365
                )
        )
        sn = (
                sum = 3
                stepbetween = 600
        )
        pacing = (
                types = 2
                s1 = (
                        sum = 6
                        stepbetween = 100
                        start = 100
                        automation = -1
                )
                s2 = (
                        sum = 6
                        stepbetween = 90
                        start = 120
                        automation = 1
                )
        )
        calcdipole = yes
        calccardiacvectorloop = no
)
```

Listing 1. Configuration for AF simulation.

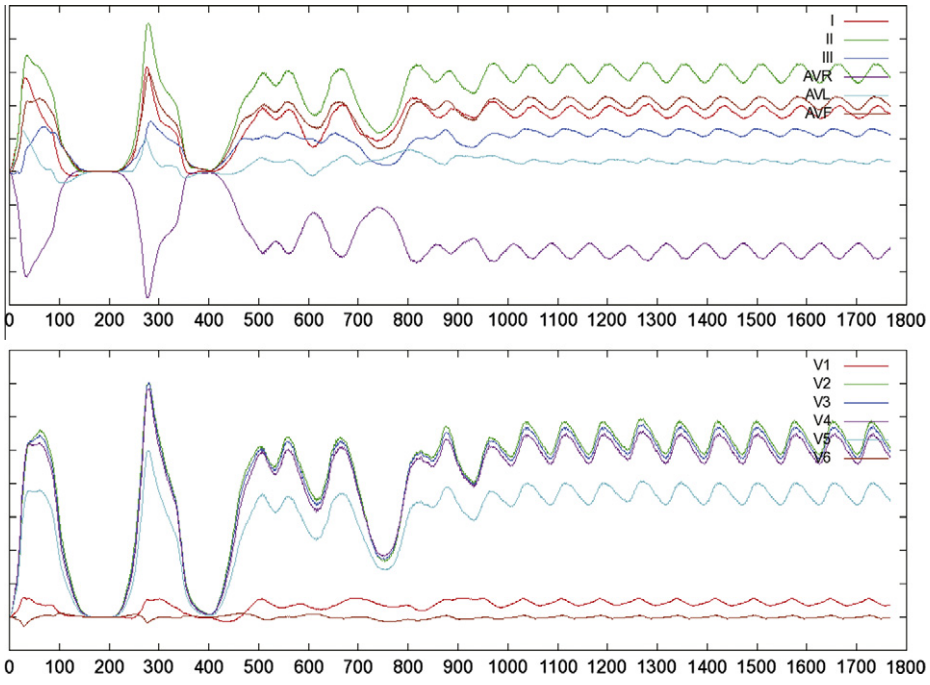

Fig. 11. ECGs waveform in limb leads (I, II, III, AVR, AVL, AVF) and precordial leads (V1–V6) in AF simulation. *X* axis denotes time in ms.

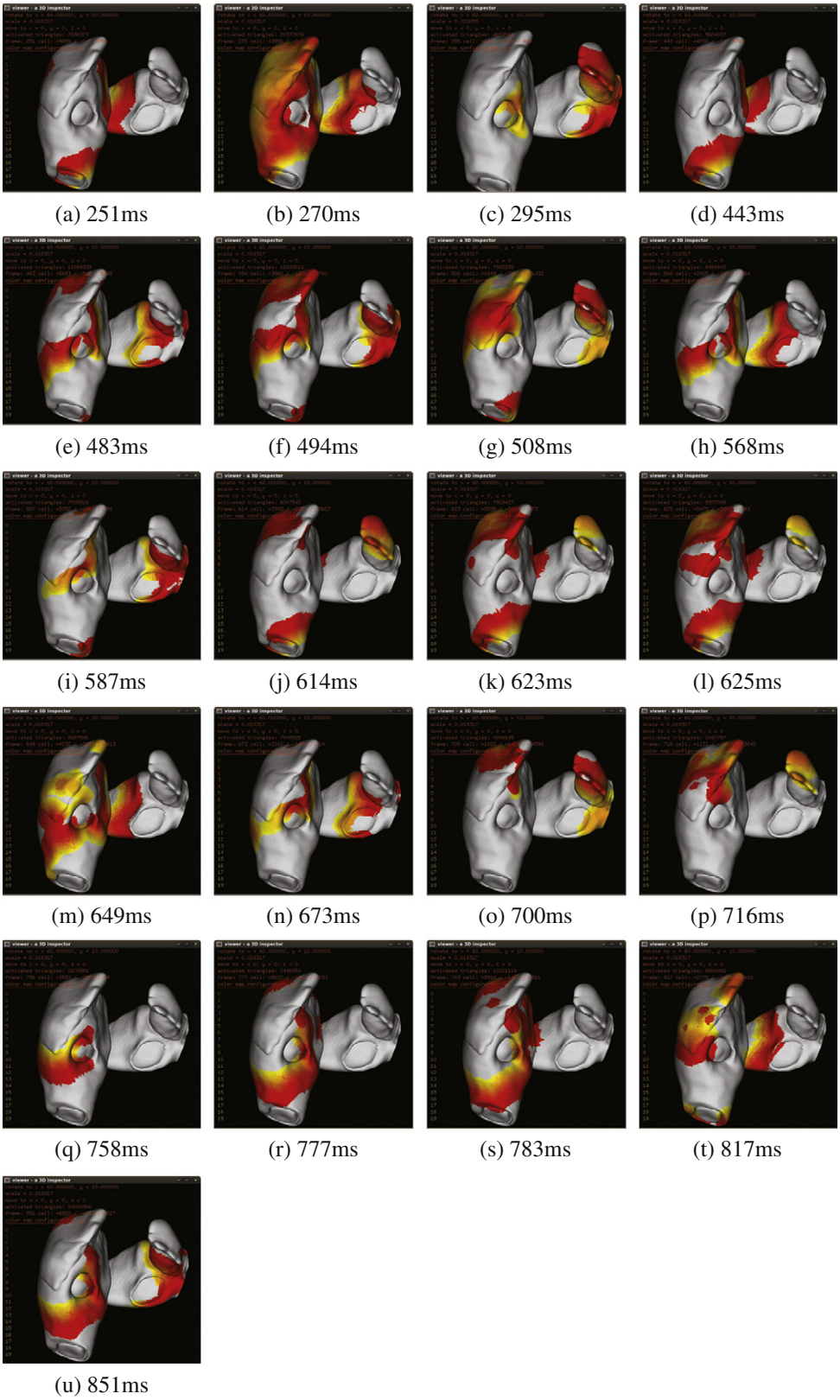

Fig. 12. (a)–(u) Gives the isochronal maps of wavefront propagation from 1–851 ms in an AF, These isochronal maps depicts the generation of the main reentry by several ectopic foci.

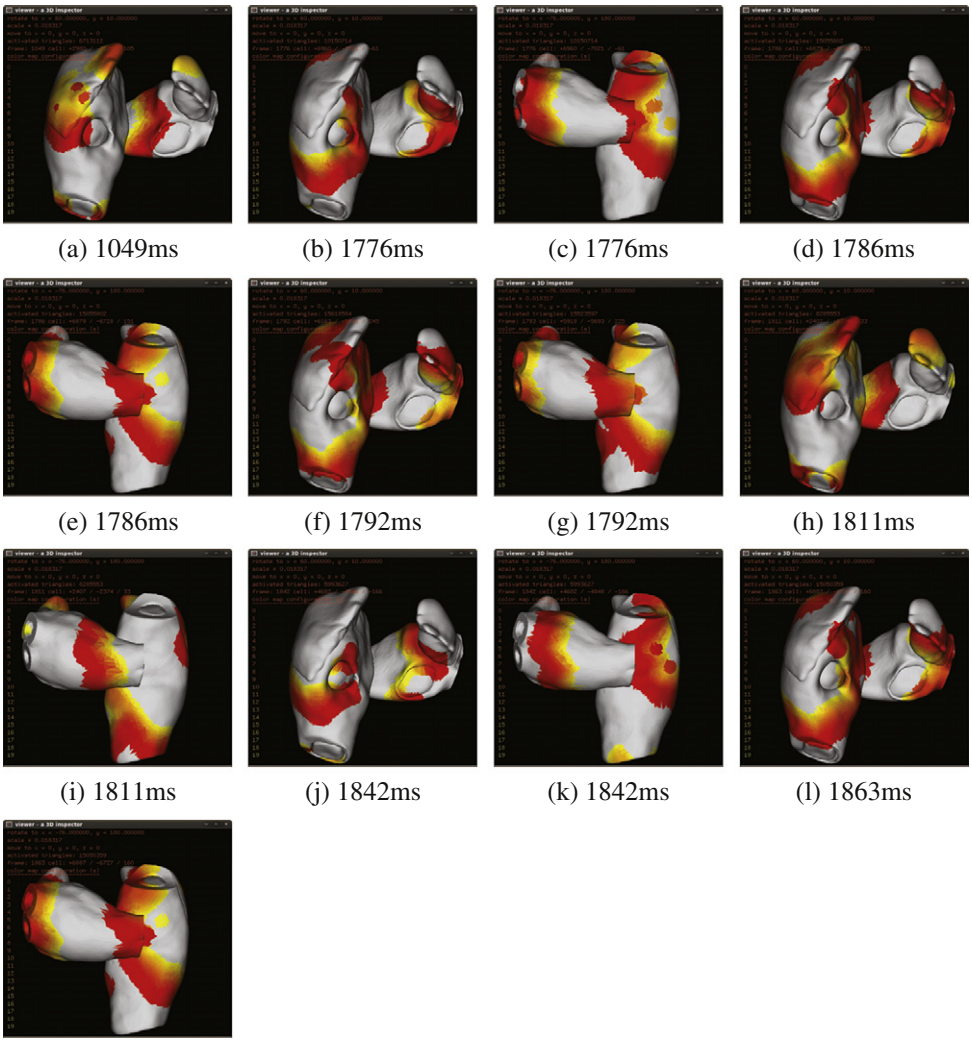

(a) 1049ms (b) 1776ms (c) 1776ms (d) 1786ms

(e) 1786ms (f) 1792ms (g) 1792ms (h) 1811ms

(i) 1811ms (j) 1842ms (k) 1842ms (l) 1863ms

(m) 1863ms

Fig. 13. (a)–(m) Gives the isochronal maps of wavefront propagation from 1049 ms to 1863 ms in the same AF. These isochronal maps demonstrate the morphology of the main reentry.

5. Discussion

5.1. Perspective view, isochronal map and ECGs

When we analyse the propagation of activation in the sinus rhythm, we use the perspective propagation investigation and isochronal map as a complementary strategy, which are generated by the viewer in this computational model. The perspective propagation investigation could indicate the traversing of impulse along intracardiac structures, e.g. Bachmann bundle (Fig. 7e). Unfortunately, this method could sometimes, especially in AF case, dim the wavefront on the frontal epicardial surface because the propagation on the posterior part is projected through the translucent scene. On the other hand, isochronal map could vividly represent the locations of wavefront on the frontal epicardial surface in a short time window. From this point of view, our model introduces both methods. ECG waveform, a commonly used clinic diagnosis standard, is also included in our model.

5.2. The estimation error caused by the Huygen's principle

In modern computer model, action potential generation and propagation are usually described as reaction–diffusion systems(Eq. (16)) [9], where C_m is a capacity of membrane, I_{ion} is the total sum of inward and outward current, α is the fiber radius and r_i is the axial resistance per unit length. The resistance r_i here corresponds to an average resistance of the intracellular space, including cytoplasmic and gap junctional resistances. The right side of this equation could be omitted (=0), if only one cell is under consideration. The cell model, e.g. Nygren's atrium model [13] is based on this simplification. But if in multiple cell's case, the transmembrane voltage waveform simulated in a certain cell is definitely different, which means the estimation error caused by the Huygen's principle could not be amended through only integrating a certain cell model. The cell model could only make the AP waveform a bit closer to the real condition comparing with the AP generation manner in Wei–Harumi's model.

$$C_m \cdot \frac{\partial V_m}{\partial t} + I_{ion} = \left(\frac{\alpha}{2r_i} \cdot \frac{\partial^2 V_m}{\partial x^2} \right) \tag{16}$$

If we have a further exploration on the source of the estimation error, we may find that in a model dominated by the Huygen's principle, the propagation of excitation between two cells is 'binary', i.e. current cell is activated as soon as its neighbor is activated in the previous simulation step. Mathematically

speaking, this means the r_i in Eq. (16) is infinitely-great in a simulation step while it is infinitely-small between continuous simulation steps. So if the size of simulation cell is chosen properly, the model based on Huygen's principle could also be able to inflect the real situation in the myocardium, because of the resistance of cytoplasm is physiologically much higher than the junction. So in this model, solid angle calculation is introduced to divide anatomic model into arbitrary size of simulation union, which can decrease the error caused by the approximation by Huygen's principle.

5.3. The limitation of this model

Unfortunately, some phenomenons could not be reproduced in this model (or in some models based on reaction-diffusion principle) due to the limitation in the rules we used in propagation simulation in our model. They are :

AP as well as the velocity change in the structural boundaries
collisions of APs with complete or partial boundaries could increase the local velocity of conduction as well as the shape of AP [38,39], because the axial current will be reflected at the boundary.

Velocity in the wavefront of activation should not be constant
the velocity in the front of curved wavefront is less than the velocity in the non-curved wavefront because of the more sinks existed in the curved wavefront [40]. A conduction will not even sustained below a critically small radius.

Velocity distribution caused by the different shape of cell
different cells have different shapes, e.g. 'brick stone' like in audit ventricular myocytes, 'fusiform' like in neonatal myocytes and SN node cell. The shape variation will cause the anisotropic of connection (CX43 and CX40), which will finally cause a distribution of velocity in myocardium.

In our model, velocity is only classified into three categories: bundle, bulk and slowregion, which is not adaptable to the structural boundaries, the curved of wavefront as well as the cell shape, so our model could not simulate these phenomena.

6. Conclusion

In this paper, we present a well designed solution for computational electrophysiological simulation, and the source code of which is available at http://cardiacsimu.sourceforge.net. This computational model is directly derived from several studies [2,3,5]. Strengths of these systems, such as the special conduction system in Harrild model and Vigmond model, the propagation simulation based on Huygens's principle in Wei–Harumi model, are well taken to evolve into a totally new one, e.g. adding partition method based on including test.

This computational model is capable of generating result for clinic study, e.g. ECG waveforms, isochronal map, perspective propagation investigation, as demonstrated in two experiments. The result of first experiment in sinus rhythm is identical to the outcome of Harrild et al.'s study [2] as well as some former clinic measurements [35] and electrophysiological theories [36,37], and could be used as the verification of the whole model. In the other experiment, two trains of boost pacing are acted alternatively on RSPV and IVC, a foci triggered AF is observed on the epicardial surface.

Acknowledgments

The authors would like to thank the valuable contributions of BodyParts3D project team for their open accessible anatomic data.

References

[1] Andrea N, Jose J. Atrial fibrillation: from bench to bedside. Humana Press; 1994.
[2] Harrild DM, Henriquez CS. A computer model of normal conduction in the human atria. Circ Res 2000;87:25–36.
[3] Wei D. Whole-heart modeling:progress, principles and applications. Prog Biophys Mol Biol 1997;67:17–66.
[4] Cherry EM, Xie F, Feliciano Z, Garfinkel A. Computer modeling of atrial fibrillation. Card Electrophysiol Rev 2001;5:271–6.
[5] Vigmond EJ, Ruckdeschei R, Trayanova N. Reentry in a morphologically realistic atrial model. J Cardiaovascular Electrophysiol 2001;12:1046–54.
[6] Seemann G, Hoper C, Sachse FB, Dossell O, Holden AV, Zhang H. Heterogeneous 3D anatomical and electrophysiological model of human atria. Philos Trans Roy Soc 2006;364:1465–81.
[7] Gavaghan D, Garny A, Maini PK, Kohl P. Mathematical models in physiology. Philos Trans Roy Soc 2006;364:1099–106.
[8] Hodgkin A, Huxley A. A quantitative description of membrane current and its application to conduction and excitation in nerve. J Physiol 1952;117:500–44.
[9] Kleber AG, Rudy Y. Basic mechanisms of cardiac impulse propagation and associated arrhythmias. Physiol Rev 2004;84:431–88.
[10] Wei D, Okazaki O, Harumi K, Harasawa E, Hosaka H. Comparative simulation of excitation and body surface electrocardiogram with isotropic and anisotropic computer heart models. IEEE Trans Biomed Eng 1995;42:343–57.
[11] Ryzhii E, Wei D. Computer simulation of atypical brugada syndrom. J Electrophysiol 2009;42:319–27.
[12] Xin Z, Wei D. Computer simulation of intracardiac potential with whole heart model. Int J Bioinform Res Appl (IJBRA) 2007;3:100–22.
[13] Nygren A, Fiset C, Firek L, Clark JW, Lindblad DS, Clark RB, et al. Mathematical model of an adult human atrial cell, the role of k+ currents in repolarization. Circ Res 1998;82:63–81.
[14] Mitsuhashi N, Fujieda K, Tamura T, Kawamoto S, Takagi T, Okubo K. BodyParts3D: 3D structure database for anatomical concepts. Nucl Acids Res 2009;37:782–5.
[15] Opstream AV, Strackee J. The solid angle of a plane triangle. IEEE Trans Biomed Eng 1983;30:125–6.
[16] Ronald DB. Electrical restitution hysteresis: good memory or delayed response? Circ Res 2004;94:567–9.
[17] Byung SK, Yong HK, Gyo SH, Hui NP, Sang CL, Wan JS, et al. Action potential duration restitution kinetics in human atrial fibrillation. J Am Coll Cardiol 2002;39:1329–36.
[18] Sanjiv MN, Dhruv K, David EK, Wounter JR. Repolarization and activation restitution near human pulmonary veins and atrial fibrillation initiation: a mechanism for the initiation of atrial fibrillation by premature beats. J Am Coll Cardiol 2008;52:1222–30.
[19] Raitt M, Kusumoto W, Giraud G. Electrophysiologic predictors of the recurrence of persistent atrial fibrillation within 30 days of cardioversion. Am J Cardiol 2004;93:107–10.
[20] Gong YF, Xie F, Stein KM, Garfinkel A, Culianu CA, Lerman BB, et al. Mechanism underlying initiation of paroxysmal atrial flutter/atrial fibrillation by ectopic foci. Circulation 2007;115:2094–102.
[21] Xie F, Qu Z, Garfinkel A, Weiss JN. Electrical refractory period restitution and spiral wave reentry in simulated cardiac tissue. Am J Physiol Heart Circ 2002;283:448–60.
[22] Cherry EM, Evans SJ. Properties of two human atrial cell models in tissue: restitution, memory, propagation, and reentry. J Theor Biol 2008;254:674–90.
[23] Schwan HP, Kay CF. Capacitive properties of body tissues. Circ Res 1975;5:439–43.
[24] Plonsey R, Heppner DB. Considerations of quansi-stationarity in electrophysiological systems. Bull Math Biophys 1967;29:657–64.
[25] Miller WT, Geselowitz DB. Simulation studies of the electrocardiogram. I. The normal heart. Circ Res 1978;43:301–15.
[26] Rudy Y, Plonsey R. The eccentric spheres model as the basis for a study of the role geometry and inhomogeneities in electrocardiography. IEEE Trans Biomed Eng 1979;26:392–9.
[27] Aoki M, Okamoto Y, Musha T, Harumi K. Three dimensional simulation of the ventricular depolarization and repolarization processes and body surface potentials: normal heart and bundle branch block. IEEE Trans Biomed Eng 1987;34:454–62.
[28] Gnuplot homepage. <http://www.gnuplot.info>.
[29] The gtk+ project. <http://www.gtk.org>.
[30] OpenGL. <http://www.opengl.org>.
[31] GNU General Public License. <http://www.gnu.org/licenses/gpl.html>.
[32] GNU Compiler Collection. <http://gcc.gnu.org>.
[33] GNU Make. <http://www.gnu.org/software/make>.

[34] Gamma E, Helm R, Johnson R, Vlissides JM. Design patterns: elements of reusable object-oriented software. Addison-Wesley; 1994.
[35] Durrer D, Van Dam RT, Freud GE, Janse MJ, Meijler FL, Arzbaecher RC. Total excitation of the isolated human heart. Circulation 1970;41: 899–912.
[36] Malmivuo J, Plonsey R. Bioelectromagnetism: principles and applications of bioelectric and biomagnetic fields. Oxford University Press; 1995.
[37] Havmoller R, Carlson J, Holmqvist F, Herreros A, Meurling CJ, Olsson B, et al. Aged-related changes in p wave morphology in healthy subjects. BMC Cardiovasc Disord 2007;7:22.
[38] Spach MS, Barr RC, Serwer GS, Johnson EA, Kootsey JM. Collision of excitation waves in the dog purkinje system: extracellular identification. Circ Res 1971;24:499–511.
[39] Spach MS, Kootsey JM. Relating the sodium current and conductance to the shape of transmembrane and extracellular potentials by simulation: effects of propagation boundaries. IEEE Trans Biomed Eng 1985;32:743–55.
[40] Fast VG, Kleber AG. Cardiac tissue geometry as a determinant of unidirectional conduction blocks: assessment of microscopic excitation spread by optical mapping in patterned cell cultures and in computer model. Cardiovasc Res 1995;29:697–707.